

## TYPE III EXCITABILITY, SLOPE SENSITIVITY AND COINCIDENCE DETECTION

XIANGYING MENG\*

Dynamics and Control, Beihang University, Beijing, China  
Center for Neural Science, New York University, USA

GEMMA HUGUET\*

Center for Neural Science, New York University, USA  
Centre de Recerca Matemàtica, Barcelona, Spain

JOHN RINZEL

Center for Neural Science, New York University, USA  
Courant Institute of Mathematical Sciences, New York University, USA

**ABSTRACT.** Some neurons in the nervous system do not show repetitive firing for steady currents. For time-varying inputs, they fire once if the input rise is fast enough. This property of phasic firing is known as Type III excitability. Type III excitability has been observed in neurons in the auditory brainstem (MSO), which show strong phase-locking and accurate coincidence detection. In this paper, we consider a Hodgkin-Huxley type model (RM03) that is widely-used for phasic MSO neurons and we compare it with a modification of it, showing tonic behavior. We provide insight into the temporal processing of these neuron models by means of developing and analyzing two reduced models that reproduce qualitatively the properties of the exemplar ones. The geometric and mathematical analysis of the reduced models allows us to detect and quantify relevant features for the temporal computation such as nearness to threshold and a temporal integration window. Our results underscore the importance of Type III excitability for precise coincidence detection.

**1. Introduction.** The nonlinear dynamics of neuron models and neurons have intrigued us for decades. The mathematical characterization of firing properties is highly developed although even for some simple exemplar models we are uncovering new questions and behaviors (see [16]). Here, we recall Hodgkin's classification in 1948 of repetitive firing behaviors (3 classes) based on accumulated empirical evidence for steady inputs to various axon types [15]. We will focus on some features of Class 3 - systems that do not fire repetitively and contrast their potential for exquisite temporal precision with that of systems that can fire repetitively.

In 1979, Rinzel and Ermentrout provided the mathematical framework that relates to two of the three classes [16, 30]. They defined Types I and II, in analogy to Hodgkin's Classes I and II, in terms of different bifurcations from stable steady state to periodic behavior as the stimulus parameter was varied. For Type I, the

---

2000 *Mathematics Subject Classification.* Primary: 92C20 , Secondary: 37N25 .

*Key words and phrases.* Type-III excitability, coincidence detectors, fast-slow systems, phase-locking, neuronal dynamics.

\* X.M. and G.H. contributed equally to this work.

transition involves the appearance of a stable limit cycle from a saddle-node on an invariant circle. For Type II, the steady state loses stability and repetitive firing emerges from a Hopf bifurcation. The mathematical classifications are local, based on the onset of repetitive activity, and were developed for point neuron models. The Hodgkin-Huxley (HH) model is Type II (see, eg, [16, 28]) while the Wang-Buzsaki model [40], often used for cortical neurons, is Type I. Rinzel and Ermentrout [30] demonstrated with a two-variable HH-like model, adapted from Morris and Lecar's formulation for barnacle muscle electrical activity, that the model can be tuned with different parameter settings to be Type I or Type II. Some cortical neurons are reported by Tateno *et al* [39] to fall into the classification scheme of Types I and II.

Although many neurons and neuron models that have stable resting states will fire repetitively for adequate steady input, some neurons and models do not fire repetitively for any steady or slowly varying inputs. They fire only one or a few spikes at the onset of a steady stimulus. This behavior is compatible with Hodgkin's Class III and has been referred to as Type III excitability [5, 16, 24]. Such "phasic" firing (vs "tonic" or repetitive firing) underlies the functional description of these units as differentiators or slope-detectors. They can encode the occurrence and time of rapid change in the stimulus. Some examples include: auditory brain stem neurons that are involved with precise timing computations [4, 33], some spinal cord neurons [23, 24], and the squid giant axon [5].

Yes, healthy squid giant axon is typically phasic. It fires one spike, maybe a few spikes, at the onset of a current step applied to an excised axon [5]. When intact, the axon delivers a brief response that triggers the squid's escape behavior, sudden contraction of the mantle muscle (see the video "The squid and its giant nerve fiber" filmed in 1970 at Plymouth Marine Laboratory (England), [www.science.smith.edu/departments/NeuroSci/courses/bio330/squid.html](http://www.science.smith.edu/departments/NeuroSci/courses/bio330/squid.html)) - with no apparent need for repetitive firing. Thus, the standard HH model, which is Type II [28], is at odds with such experimental observations. On the other hand, the squid axon when bathed in lowered calcium seawater can fire repetitively and has been useful as a model for Type II behavior [14].

What underlies Type III excitability? The slope sensitivity relies, speaking generally and qualitatively, on a dynamic subthreshold negative feedback mechanism. In order for a phasic neuron to fire, the input and the rise in voltage must be fast enough so that little negative feedback is recruited. For slow inputs the negative feedback keeps pace with the voltage and prevents the neuron from reaching spike threshold. Hence the time scale (fast enough but not too fast) and voltage sensitivity (recruitable in the subthreshold regime) of such negative feedback are key biophysical factors.

Among top contenders for the "definitive Type III neuron" for temporal precision are the brain stem neurons (in the medial superior olive, MSO) that compute the interaural time difference for sound localization. MSO neurons are highly specialized for this computation. They are endowed with fast membrane time constants and synapses with fast dynamics and they perform coincidence detection (for inputs from the two ears) to a resolution of tens of microseconds [1, 13]. While cortical neurons may have integration and excitatory synaptic time scales of tens and a few milliseconds, respectively, the corresponding time scales for MSO neurons are sub-milliseconds. But this speed alone is not enough to explain the temporal precision of sound localization. MSO neurons exhibit one or more dynamic subthreshold

negative feedback mechanisms [3, 19, 25, 37, 38]. The negative feedback's time scale is comparable to the neuronal time constant, enabling the feedback to compete temporally with the voltage rise and to preclude spiking if the rise is just a little bit too slow. A leading biophysical contributor to the negative feedback and phasic firing property of some auditory brain stem phasic-firing neurons, including in MSO, is a potassium current that activates with voltage below the threshold for spike generation [19, 25, 37]; a widely used model is due to Rothman and Manis, based on their voltage-clamp data [32]. We will refer to this model as RM03. Interestingly, the modeling and experimental work of Clay to align the HH-model with the phasic firing property of squid axons fingers the axon's potassium current which if shifted somewhat to activate at lower voltages than originally formulated can convert the HH model from Type II to Type III [5]. Shifted potassium activation was also used in [24] to create a subthreshold negative feedback.

In this paper we will highlight some distinctive features of phasic firing in terms of dynamical systems theory. While using the RM03 model for illustration we will introduce idealized models that have similar features, thereby demonstrating generality. As a function of a steady input's amplitude a Type III neuron model (in the purest sense), such as the RM03 model, shows no bifurcation to repetitive activity no matter how large is the amplitude. The RM03 phasic model exhibits highly precise phase locking and coincidence-detecting properties as compared to a tonic version of RM03. Here, we pose the coincidence-detection problem as an idealization of the computation done by MSO neurons. There are two inputs – each is a half-wave rectified sine-wave, say frequency 100 Hz or so, as if one stimulus is coming from a pure tone input to each ear and representing the mean excitatory drive from several nerve fibers that carry spikes activated by the cochlear nerve. We ask how the firing depends on the phase difference between the two stimuli, ISPD (Interstimuli Phase Difference). For a noise-free input this leads to the question of phase-locking posed for a time-shifted but otherwise identical stimulus pair. For small ISPD the model will fire a single spike per cycle but for ISPD, say  $\pm 0.5$  there is no firing. When we add noise to represent the small jitter in spike arrival times we plot firing probability vs ISPD to obtain the model's tuning curve for ISPD. The tonic model has poor selectivity compared to the phasic model. The Type III models, as slope detectors, show a strong preference for firing at the sharply rising phases of a periodic signal while the tonic model fires in a broad temporal window near the signal's peak amplitude. To gain insight into the temporal window for firing we developed a reduced two-variable version of the eight-variable RM03 model; this model retains many of the biophysical features of RM03 and semi-quantitatively agrees with RM03. By using phase plane analysis we characterize the window of opportunity for firing as the time-varying signal modulates the nullclines and the effective firing threshold separatrix (even though the resting state is stable for each value of the stimulus). Finally we study an idealized integrate-and-fire model with a threshold that depends on time and voltage, rising with voltage in the subthreshold regime.

## 2. Results.

**2.1. Rothman and Manis model.** Rothman and Manis [32] developed a Hodgkin-Huxley-like neuron model that has been widely used for modeling the phasic firing of cells in the auditory brainstem (see Table I, Type II in [32]). It consists of a sodium current  $I_{Na}$ , a high-threshold ( $I_{KHT}$ ) and a low-threshold ( $I_{KLT}$ ) potassium

currents, a hyperpolarization-activated cation current  $I_h$  and a leak current  $I_{lk}$ . The current balance equation is:

$$C_m \frac{dV}{dt} = -I_{Na} - I_{KHT} - I_{KLT} - I_h - I_{lk} + I(t), \quad (1)$$

where  $C_m$  is the membrane capacitance,  $V$  is the membrane voltage and  $I(t)$  is the input current. Each ionic current  $I_i$  is governed by an activation and/or inactivation variable, and equation (1) can be written as

$$C_m \frac{dV}{dt} = 2[-\bar{g}_{Na}m^3h(V - E_{Na}) - \bar{g}_{KHT}(0.85n^2 + 0.15p)(V - E_K) - \bar{g}_{KLT}w^4z(V - E_K) - \bar{g}_hr(V - E_h) - \bar{g}_{lk}(V - E_{lk})] + I(t), \quad (2)$$

where  $\bar{g}_i$  and  $E_i$  are respectively the maximal conductances and reversal potentials for the ionic current  $i = Na, KHT, KLT, h, lk$ . We use the same parameter values as in [32], except that maximal conductances and channel gating rates are multiplied by a factor of 2 and 3, respectively, as in [11], to mimic the brain slices during whole cell recordings at temperature  $32^\circ C$ . Membrane capacitance is  $C_m = 12$  pF; maximal channel conductances are  $\bar{g}_{Na} = 1000$  nS,  $\bar{g}_{KHT} = 150$  nS,  $\bar{g}_{KLT} = 200$  nS,  $\bar{g}_h = 20$  nS and  $\bar{g}_{lk} = 2$  nS and reversal potentials are  $E_{Na} = 55$  mV,  $E_K = -70$  mV,  $E_h = -43$  mV and  $E_{lk} = -65$  mV.

The dynamics for activation and inactivation variables is described by the following differential equation:

$$\frac{dx}{dt} = 3 \frac{x_\infty(V) - x}{\tau_x(V)} \quad (3)$$

where  $\tau_x$  is the time constant of the variable  $x = m, h, n, p, w, z, r$  and  $x_\infty(V)$  is the steady-state value of  $x$  at a fixed voltage  $V$ . The expressions for  $x_\infty(V)$  and  $\tau_x(V)$  are obtained experimentally from voltage-clamp responses and are given in [32].

Of particular interest for our problem is the low-threshold potassium current  $I_{KLT}$  which is primarily responsible for the Type III behavior of the neuron. The  $I_{KLT}$  current is partially activated at the resting state (see Fig. 9 in Appendix A). When the cell is depolarized the steady state  $w_\infty$  of the activation variable  $w$  also rises (see Fig. 9) and the activation variable approaches this value with a time constant  $\tau_w$  that at rest is comparable to the membrane time constant. If the membrane potential changes slowly  $I_{KLT}$  has enough time to activate adequately and prevent the generation of a spike. On the contrary, if  $V$  changes fast the system can reach the spike threshold before  $I_{KLT}$  current has time to activate. During the spike, the system can recruit enough  $I_{KLT}$  to prevent any further spiking.

In order to emphasize the distinctive features of phasic firing and Type III excitability, we manipulated the model so that it fires tonically for a steady input, converting it to Type II excitability. We disabled the subthreshold dynamic negative feedback by freezing the conductance (activation and inactivation variables  $w$  and  $z$ ) of  $I_{KLT}$  to its value at the resting state as in [7]. This manipulation converts the model from phasic to tonic, keeping the same membrane time constant and input resistance. Moreover, the maximal sodium conductance  $\bar{g}_{Na}$  is increased from 1000 nS to 1500 nS, in order to increase the size of the spikes (amplitude of the limit cycle) and the range of inputs that generate repetitive firing (range of  $I$  for which a stable limit cycle exists) as in [12].

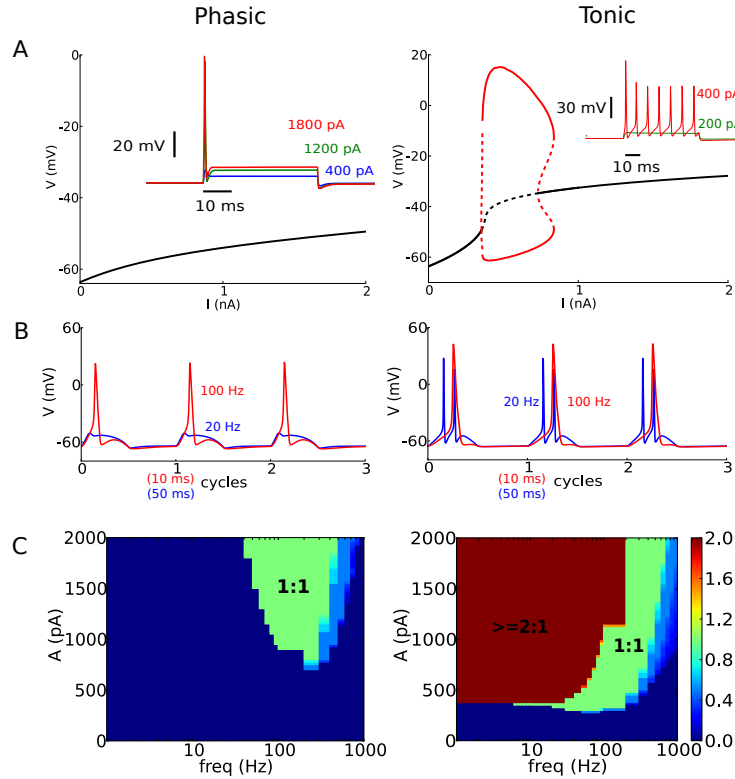


FIGURE 1. Dynamic response properties of the RM03 model. (A) Bifurcation diagrams of the phasic (left) and tonic (right) RM03 models for a steady current  $I$ . Solid lines represent stability and dashed lines instability. Black lines represent fixed points and red lines the maximum and minimum values of periodic orbits. The inset shows the voltage responses to a 40 ms-duration step current of different amplitudes (400 pA, 1200 pA, 1800 pA for the phasic model and 200 pA and 400 pA for the tonic model). (B) and (C) Responses of the phasic (left) and tonic (right) models to a half-wave rectified sinusoid input. (B) Time course of the membrane potential over three periods in response to a half-wave rectified sinusoid input of frequencies 20 Hz (blue trace) and 100 Hz (red trace) and amplitudes 1200 pA (phasic model) and 400 pA (tonic model) (C) Frequency-response maps of the models for a half-wave rectified sinusoid input with varying frequency (x-axis) and amplitude (y-axis). Colors indicate number of spikes per cycle.

2.1.1. *Phasic vs tonic behavior.* In Fig. 1 we show the responses of the phasic (left column) and tonic (right column) models to a step current (inset Fig. 1A) and a half-wave rectified sinusoidal input (B and C).

In response to a step of current (constant for  $t_{\text{on}} < t < t_{\text{off}}$  and zero otherwise), the phasic RM03 model fires only once (if at all) at the onset of the stimulus and not thereafter (inset Fig. 1A left). For RM03, the steady state is stable for any

value of a steady current  $I$  (Fig. 1A left). The onset spike is due to transient dynamics before the system reaches the steady state. This is the so-called Type III excitability.

In contrast, tonic neurons show repetitive firing when the amplitude of the stimulus is above a certain threshold (inset Fig. 1A right). Indeed, when the cell is depolarized enough the resting state destabilizes and stable oscillations emerge (see bifurcation diagram in Fig. 1A right). Since in our model this transition occurs through a Hopf bifurcation, the system is Type II. Repetitive firing is possible for moderate values of  $I$ , but for  $I$  too large the limit cycle disappears through a sub-critical Hopf bifurcation and the highly-depolarized state becomes stable. This is known as nerve block.

**2.1.2. Slope detectors vs amplitude detectors.** For time-varying inputs, tonic and phasic models respond differently. The contour plots in Fig. 1C show the number of spikes per cycle in response to a single half-wave rectified sinusoidal input  $I(t)$  with amplitude  $A$  and frequency  $\omega$ ,

$$I(t) = A[\sin(2\pi\omega t)]^+, \quad (4)$$

where  $[\cdot]^+ = \max(\cdot, 0)$ . Since hair cells tend to respond to unidirectional fluctuations, this input idealizes the mean excitatory drive to MSO neurons when a pure tone is presented to one ear [1]. This description is valid for low frequencies (less than 1-2 kHz).

For the tonic model the minimal amplitude  $A$  for firing is relatively constant for low frequencies (Fig. 1C right) – around 360 pA, where the Hopf bifurcation occurs (see bifurcation diagram Fig. 1A right). In contrast, for the phasic model the minimal amplitude for firing is strongly frequency dependent, rising abruptly as frequency decreases below 100 Hz (Fig. 1C left). There is no firing for low frequencies. Indeed, phasic neurons respond to such inputs only if the amplitude and frequency are high enough (but not too high), that is, when input rises faster than a certain threshold. For this reason phasic neurons are often called slope detectors.

Again phasicness is observed in the spiking ratio (spikes per cycle). For low-frequency inputs, the tonic model fires more than 1 spike per cycle whereas the phasic model fires only once if at all, even when the amplitude is increased. Fig. 1B shows voltage time courses, responses for two representative frequencies, slow and moderate.

**2.1.3. InterStimulus Phase Difference (ISPD) tuning curves.** Next we compare the ability of tonic and phasic neurons to detect coincident inputs. To do so, we consider two inputs, each is a half-wave rectified sinusoid representing the mean excitatory drive originated by a pure tone input at each ear, and we compute the firing rate probability as a function of the phase difference  $\Delta_P$  between them. We call this function the InterStimulus Phase Difference (ISPD) tuning curve. The injected current, allowing for noise to represent the small jitter in input arrival times, takes the form

$$I(t) = A([\sin(2\pi\omega t)]^+ + [\sin(2\pi\omega t + 2\pi\Delta_P)]^+) + \sigma\eta(t), \quad (5)$$

where  $\eta(t)$  is a white noise process with zero mean and unit variance  $\langle \eta(t)\eta(t') \rangle = \delta(t - t')$ .

Notice that the input shape ranges from a half-wave rectified sinusoid with double amplitude when both inputs arrive together ( $\Delta_P = 0$ ) to a double bump with no

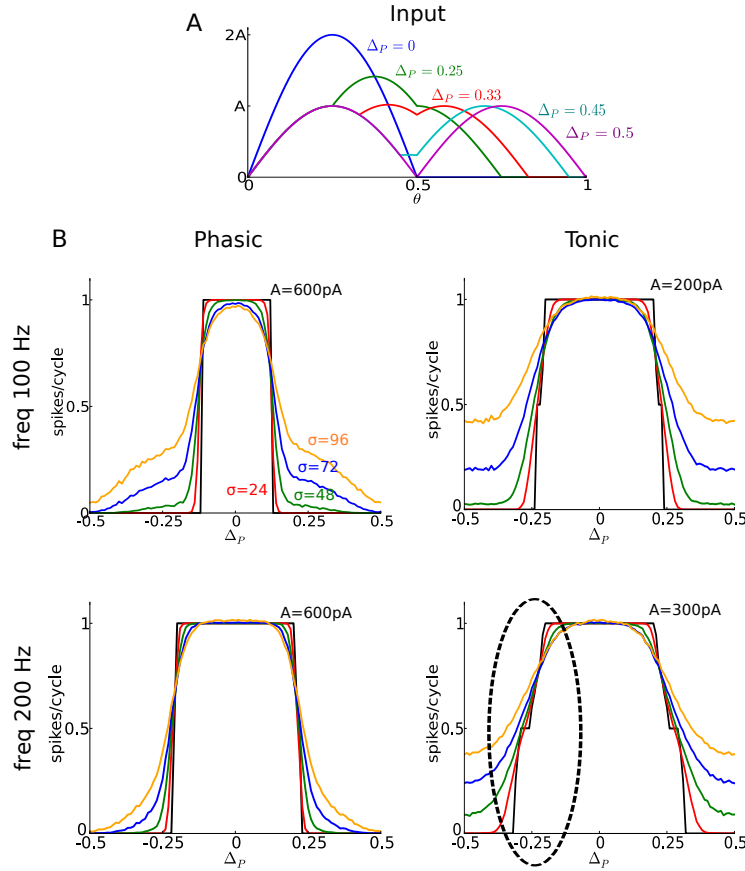


FIGURE 2. Coincidence detection tuning properties of the RM03 model. (A) Time course of the input signal over one period for different phase shifts  $\Delta_P$ . (B) Interstimuli Phase Difference tuning curves for phasic (left) and tonic (right) models. Plots show the spiking ratio (spikes/cycle) in response to an input current consisting of two half-wave rectified sinusoids with varying phase shift  $\Delta_P$  for the deterministic case (black curve) and for different levels of noise ( $\sigma = 24$  pA, 48 pA, 72 pA, 96 pA corresponding to red, green, blue and yellow curves respectively). The frequencies for a single half-wave rectified sinusoid are 100 Hz (top) and 200 Hz (bottom) and the amplitudes are indicated in each panel. The circled region in the 200 Hz tonic panel draws attention to a devil's staircase for the noise-free tonic model.

pause when they arrive out of phase ( $\Delta_P = 0.5$ ) (Fig. 2A). For our simulations we chose a frequency and amplitude for which a single input to the noise-free model does not cause firing but with both inputs present and in-phase there is one firing per cycle.

The shape of the ISPD is determined by slope sensitivity in the case of the phasic model and by amplitude sensitivity for the tonic model. Indeed, Fig. 2B shows that for the noise-free phasic model there is a sudden drop from 1 to 0 which



occurs around  $\Delta_P = 0.1$  for frequency 100 Hz and  $\Delta_P = 0.2$  for frequency 200 Hz. These  $\Delta_P$  values correspond to a time difference  $\Delta_T$  between the two inputs of the order of 1 ms. This critical  $\Delta_T$  decreases moderately over a certain range as the frequency increases (results not shown).

For the tonic model this drop occurs around  $\Delta_P = 0.25$  for  $f = 100$  Hz and  $A = 200$  pA and around  $\Delta_P = 1/3$  for  $f = 200$  Hz and  $A = 300$  pA. This corresponds to a signal whose maximal amplitude is around  $A = 300$  pA. Hence, it is the stimulus amplitude that determines the drop of the ISPD tuning curve.

To illustrate the phasic model's superior sensitivity for detecting small time differences, we focus on the ISPD for a 200 Hz input (Fig. 2). In the deterministic phasic model the drop in the firing rate (spikes/cycle) from 1 to 0 occurs in less than  $50 \mu\text{s}$ , whereas for the tonic model the same drop occurs when the time difference is of the order of  $500 \mu\text{s}$ . Notice that the ISPD tuning curve for the tonic model with a 200 Hz input shows a devil's staircase over the range where the drop occurs – the tonic model phase locks with the periodic input with skipping cycles at different ratios and the simplest rational numbers have the largest steps (see circled region in Fig. 2). With noisy input, the phasic model still outperforms the tonic model. For example, for  $\sigma = 48$  pA, the phasic model's firing rate drops more than 50 % (from 0.75 to 0.33 spikes per cycle) in  $150 \mu\text{s}$ , whereas in the tonic model the same drop occurs in  $500 \mu\text{s}$ .

The ISPD tuning curves show that in the presence of noise the tonic model has relatively poor selectivity at larger ISPDs. For the phasic model the firing probability is low in the tuning curve's tails. However for the tonic model the tails are high and flat for values of  $\Delta_P$  which are over  $1/3$ . This is understandable, since for  $\Delta_P \in [1/3, 0.5]$  the maximal amplitude of  $I(t)$  is constant at the value  $A$ , the maximal amplitude of a single input. Hence, the probability of firing is the same for all ISPDs over  $1/3$ .

In contrast, the phasic model is more reliable; firing probability decreases as  $\Delta_P$  increases beyond  $1/3$ , even though the rising slope for  $I(t)$  remains constant. An important feature of the input signal plays a role here: the pause duration (the fraction of the period for which the input signal is zero). Indeed, the pause decreases linearly from  $1/2$  when  $\Delta_P = 0$  to 0 when  $\Delta_P = 0.5$ . During this pause, the  $I_{\text{KLT}}$  current that has been recruited during the depolarization is restored to its resting state value. The shorter the pause the less  $I_{\text{KLT}}$  current is removed and therefore the harder it is for the model to elicit a spike. Hence, the firing probability decreases over  $\Delta_P$ .

This shows that the phasic model is very sensitive to inputs arriving together whereas the tonic model is far less selective about how these inputs are distributed along a cycle

**2.1.4. Phase locking properties.** Neuron models with Type III excitability like RM03 can phase lock with high precision. We characterize the responsiveness by computing the firing phase and the ability of phasic neurons to phase lock with periodic inputs. To do so, we computed the firing phase and inter-spike interval (ISI) histograms for different ISPD for tonic and phasic models (see Fig. 3 for a 100 Hz input).

The firing phase histograms (usually known as period histograms in the experimental literature) show the firing rate probability as a function of the input phase. ISI histograms show the probability of a spike in a given interval of size  $\Delta t$ . To



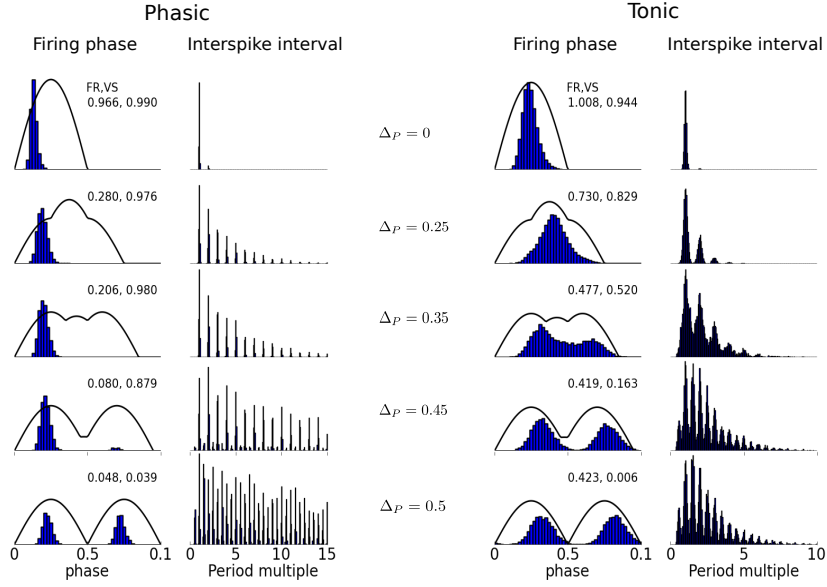


FIGURE 3. Precision of phase-locking in the RM03 model for stimulus pair with phase difference  $\Delta_P$ . Phase histograms and interspike interval (ISI) histograms for phasic (left) and tonic (right) models in response to two half-wave rectified sinusoids at different phase shifts  $\Delta_P$  with noise  $\sigma = 96pA$ . The frequency of a single half-wave rectified sinusoid is 100 Hz and the amplitude is 600 pA (phasic) and 200 pA (tonic). The curves in the phase histogram plots represent the time course of the input signal over one period. Phase histograms are normalized and the scale of the vertical axis is the same for all panels of each model. The scale of the vertical axis of the ISI histograms is different in each panel due to the large variation across panels. The numbers in the upper right corner of the phase histogram panels indicate firing rate (spikes/cycle) (FR) and vector strength (VS).

compute them we integrated the system for 20,000 cycles and we recorded the phase of the input signal at the spike times and the time between spikes, respectively.

Both the tonic and the phasic models show phase-locking with the input. However, discharges are restricted to a narrower range of phases in the phasic model. In order to measure how well the spike times are phase-locked with the periodic stimuli we compute the vector strength (VS), sometimes called “synchronization index” [13]. To compute the VS one associates to each spike a vector on the unit circle with a phase angle and computes the mean vector. The VS is given by the length of the mean vector. Notice that if the phase histogram is a delta-like distribution then  $VS=1$  (perfect locking), if it is a uniform distribution  $VS=0$  (totally asynchronous).

The phasic model locks with a higher vector strength than does the tonic model (Fig. 3). The temporal window for firing is smaller in the phasic case. It is confined to the rising phase of the depolarizing input before  $I_{KLT}$  can fully activate and prevent any further depolarization. In contrast, in the tonic case there is no

subthreshold current opposing the depolarization and therefore the stronger the depolarizing current the easier it is to trigger a spike. Hence, there exists a wide temporal window for firing around the maximum of the depolarizing input.

The tightness of phase-locking for the phasic model can be also observed in the ISI histograms (Fig. 3). Indeed, the ISIs are more tightly grouped around multiples of the period in the phasic case whereas in the tonic case there is more dispersion around them. Thus, even when some cycles are skipped the phasic model still fires with precision at preferred phase.

**2.2. V-U model.** To highlight the primary biophysical mechanisms for phasic firing properties and to facilitate our analysis, we reduced the 8-variable RM03 model to 2 variables by identifying and approximating some nonessential features for the model's excitability and spike generation mechanism. We identified three time scales: extremely fast, intermediate and slow. The activation gating variable  $m$  for  $I_{Na}$  activates extremely fast (time scale  $\ll 1$  ms), so as a first approximation we set  $m = m_\infty(V)$ . The inactivation gating variable  $z$  of  $I_{KLT}$  and the activation gating variable  $r$  of  $I_h$ , change relatively quite slow (time scales are around 100 ms or more). Since we are not interested in the influence of the continuous stimuli and  $z$  and  $r$  barely change for short-time stimuli, we freeze them at their resting states. The time scales of the membrane potential  $V$ , inactivation gating variable  $h$  of  $I_{Na}$  and activation gating variable  $w$  of  $I_{KLT}$  are intermediate and comparable (time scales are around one to a few ms). A significant feature is the near linear relationship between  $w$  and  $h$  during a spike as seen in the projection of the trajectories on the  $w - h$  plane (See Fig. 9 in Appendix B). This enables us to approximate  $w$  and  $h$  in terms of one variable  $U$ :  $h = (a/b)U$  and  $w = a(1 - U)$ . See Appendix B for more details on this reduction. A similar strategy was used by Rinzel in [29] to reduce the Hodgkin-Huxley model from four to two variables, based on FitzHugh's observation of a near linear relationship between two HH gating variables [9]. There are another two variables, the activation variables  $n$  and  $p$  of  $I_{KHT}$ , whose time scales are also intermediate. Since  $I_{KHT}$  is only recruited at high voltage ( $V > -40$  mV), the main effects of  $I_{KHT}$  are decreasing the peak and the width of the spikes, noticeable primarily for short inter-spike intervals (a few msec). The negligible influence of  $n$  and  $p$  can be seen by freezing  $n$  and  $p$  in the RM03 model. In this condition, the phase locking boundaries corresponding to the half-wave rectified sinusoid stimuli are barely changed compared with that shown in Fig. 1C (results not shown). Thus, we neglect the small contribution of  $n$  and  $p$  and we freeze them at their resting states.

Our reduced model ( $V - U$  model) is given by the following system of differential equations:

$$\begin{aligned}
 C_m \frac{dV}{dt} = & 2[-\bar{g}_{Na} m_\infty(V)^3 \left(\frac{a}{b}U\right) (V - E_{Na}) - \bar{g}_{KLT} a^4 (1 - U)^4 z_0 (V - E_K) \\
 & - \bar{g}_{KHT} (0.85n_0^2 + 0.15p_0) (V - E_K) - \bar{g}_{lk} (V - E_{lk}) - \bar{g}_h r_0 (V - E_h)] \\
 & + I(t) \\
 \frac{dU}{dt} = & 3 \frac{U_\infty(V) - U}{\tau_U(V)}
 \end{aligned} \tag{6}$$

The steady-state function  $U_\infty$  is given by

$$U_\infty(V) = \frac{b[h_\infty(V) + b(a - w_\infty(V))]}{a(1 + b^2)},$$

where  $a = 0.9$ ,  $b = (a - w_0)/h_0$  and  $\tau_U(V) = \min(\tau_w(V), \tau_h(V))$ .

Values for the gating variables, fixed at rest, are  $w_0 = 0.511$ ,  $h_0 = 0.445$ ,  $r_0 = 0.147$ ,  $z_0 = 0.662$ ,  $n_0 = 0.0077$ , and  $p_0 = 0.0011$ .

**2.2.1. Phasic vs Tonic behavior for the  $V-U$  model.** The firing behaviors of the  $V-U$  model agree with those of the RM03 model in response to a step current. The  $V-U$  model shows an onset response – only one spike, at the beginning of an adequate depolarizing current step (Fig. 4A inset). Fig. 4A shows the bifurcation diagram of the  $V-U$  model with a depolarizing current  $I$  as a parameter. The steady response is stationary; the steady state exists and is stable in the entire range of depolarizing current  $I$ . When we freeze the conductance  $g_{\text{KLT}}$  ( $g_{\text{KLT}} = \bar{g}_{\text{KLT}} a^4 (1 - U)^4 z_0$ ) of  $I_{\text{KLT}}$  at its resting level, the  $V-U$  model becomes tonic (Fig. 4A). The bifurcation diagram for the tonic  $V-U$  model (Fig. 4A) shows the range of  $I$  for which the stable limit cycle exists. Notice that the  $V-U$  model with  $g_{\text{KLT}}$  frozen shows a smaller limit-cycle range of  $I$  compared to the RM03 model (Fig. 1A). It is because the steady state inactivation function  $h_\infty$  in the  $V-U$  model decreases to 0 at a lower voltage value than that of the RM03 model as  $V$  increases. Thus, the sodium current which triggers spikes in the  $V-U$  model goes to 0 faster than that of the RM03 model during depolarization. We further tested this interpretation by steepening  $h_\infty$  in the RM03 model, and finding a smaller  $I$  range for the stable limit cycle (not shown). Nevertheless, the  $V-U$  model matches RM03 quite well.

**2.2.2. Slope detectors vs amplitude detectors.** Let us consider the effects of the dynamic change in  $I$ . The phasic  $V-U$  model, as does the RM03 model, exhibits strong sensitivity to the increasing slope of current inputs rather than to the amplitude. Fig. 4B shows the responses of the phasic  $V-U$  model to a half-wave rectified sinusoidal stimulus, equation (4), with different frequencies. With the same amplitude, the phasic  $V-U$  model does not respond to slow frequencies of the input (blue, Fig. 4B), but it fires a single spike at its rising phase for high frequencies in some range (red, Fig. 4B). See also Fig. 5A.

In contrast, the tonic  $V-U$  model shows more sensitivity to the amplitude of the stimulus rather than to the rising speed. The minimal amplitude of the tonic  $V-U$  model for spike generation remains almost the same when frequency varies, whereas for the phasic model the minimal amplitude varies a lot according to the frequency value (Fig. 5A left). Moreover, when the input amplitude is within the limit-cycle range of  $I$ , the tonic model may fire multiple spikes for low frequency sinusoidal inputs (Fig. 4B). The spikes occur near the peak of the sinusoidal stimulus. These two phenomena are also observed in the RM03 model (Fig. 1).

**2.2.3. Phase plane analysis.** Since our reduced model has only two variables we can gain further insight into the phasic properties by means of phase-plane analysis (Fig. 4C). The  $V$ -nullcline and  $U$ -nullcline are the curves along which  $dV/dt = 0$  and  $dU/dt = 0$ , respectively. The  $V$ -nullcline for the  $V-U$  model has a cubic-like shape (black, Fig. 4C), similar to many neuronal models [16, 20, 29]. The  $U$ -nullcline is decreasing sigmoid-like (green, Fig. 4C). Notice that the upper knee of the  $V$ -nullcline in Fig. 4C (tonic case for  $I=0$ pA) is clipped. For both the phasic and tonic models these two nullclines intersect on the left branch of the  $V$ -nullcline

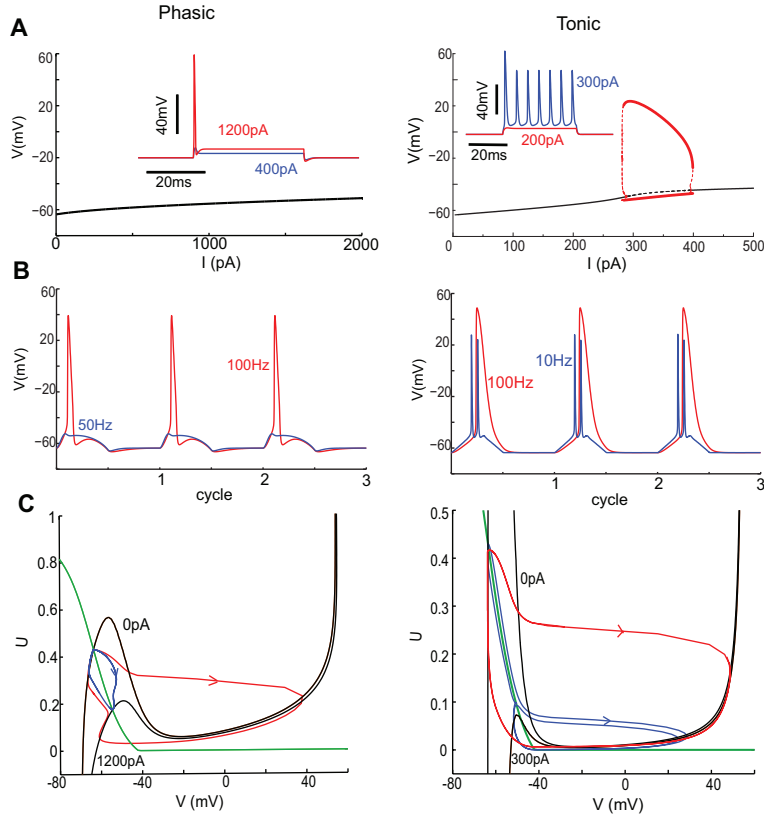


FIGURE 4. Dynamic response properties and phase plane analysis of the V-U reduction of RM03 model. (A) Bifurcation diagrams of the phasic V-U model (left) and the tonic V-U model with  $g_{KLT}$  frozen (right). Stable steady state (black solid) destabilizes at  $I = 287$  pA when  $g_{KLT}$  is frozen. Subcritical Hopf bifurcation leads to periodic orbits that stabilize for large amplitude and correspond to repetitive firing for  $I$  in the range of 287 to 396 pA (red bold line). (B) Responses of the phasic V-U model (left) and the tonic V-U model (right) to the half-wave rectified sinusoidal inputs. The frequencies of the half-wave rectified sinusoidal inputs are 100 Hz (red), 50 Hz (blue) in the left panel and 10 Hz (blue), 100 Hz (red) in the right panel. (C) phase-plane portraits corresponding to the same half-wave rectified sinusoidal stimuli as in panel B.

when there is no input,  $I = 0$  pA. This intersection corresponds to the model's stable resting state.

For both the tonic model and the phasic model increasing  $I$  as a parameter changes the cubic  $V$ -nullcline, shifting it downwards, most notably for the region around the left knee (Fig. 4C). The  $U$ -nullcline does not change with  $I$ . Eventually, for very large  $I$ , the  $V$ -nullcline becomes monotonic (not shown). However, there are differences in the phase plane portraits for the two models as  $I$  is increased.

First, the intersection of the phasic model remains on the left branch of the  $V$ -nullcline until it becomes monotonic, whereas for the tonic model, as  $I$  increases, the intersection shifts from the left branch to the middle branch. Since the intersection is stable if it is on the left branch of the  $V$ -nullcline, the steady state of the phasic  $V - U$  model never destabilizes with increasing  $I$ . On the contrary, for the tonic model the steady state destabilizes after it migrates onto the middle branch through a subcritical Hopf bifurcation (Fig. 4A and C, right); the emergent unstable periodic orbit connects to a stable limit cycle. This scenario corresponds to the transition of the tonic  $V - U$  system from a stable resting state to repetitive firing (Fig. 4A). For large  $I$ , the stable limit cycle is lost; the  $V$ -nullcline becomes monotonic and the steady state restabilizes, corresponding to nerve block.

Consider now the evolution of the phase plane as  $I$  varies according to the half-wave rectified sinusoidal input (equation (4)) in the tonic case (Fig. 4C). The steady state moves from the left branch to the middle branch during the rising phase of the sinusoid. Therefore the model can fire repetitively during a cycle if the stimulus remains long enough around its peak, in the range that corresponds to having a middle-branch intersection.

There is also a dynamic effect, primarily during the rising phase of  $I(t)$ , depending on how fast the  $V$ -nullcline moves compared to the moving phase point  $(V, U)$ . If the  $V$ -nullcline moves down fast enough to sweep downward through the moving phase point we see the conditions conducive for generating a spike. Thus there is a critical minimum rate that defines such a “dynamic criterion”. For the tonic model, it can play an additional contributing role and induce a spike even before the steady state moves onto the middle branch. For the phasic model, since the moving steady state never destabilizes, the dynamic effect is the only mechanism for generating a spike with a rising stimulus.

We can compare this dynamic effect for the two models more precisely as follows. Consider first how the  $V$ -nullcline changes as  $I$  varies. Suppose we fix  $V$  to some value and ask how the corresponding value of  $U$  on the  $V$ -nullcline changes with  $I(t)$ .

For a fixed value of  $V$  and  $t$ , the value for  $U$  on the  $V$ -nullcline satisfies the implicit equation

$$I_{\text{ion}}(V, U) - I(t) = 0,$$

where

$$I_{\text{ion}}(V, U) = 2[\bar{g}_{Na}m_{\infty}(V)^3 \left(\frac{a}{b}U\right) (V - E_{Na}) + \bar{g}_{KLT}a^4(1 - U)^4 z_0(V - E_K) + \bar{g}_{lk}(V - E_{lk}) + \bar{g}_{KHT}(0.85n_0^2 + 0.15p_0)(V - E_K) + \bar{g}_h r_0(V - E_h)]. \quad (7)$$

Since the function  $I_{\text{ion}}(V, U)$  has terms in  $U$  for  $I_{KLT}$  and  $I_{Na}$  for the phasic model and  $I_{Na}$  for the tonic model, we have that

$$\frac{\partial I_{\text{ion}}}{\partial U}(V, U) = 2 \left( \bar{g}_{Na}m_{\infty}(V)^3 \left(\frac{a}{b}\right) (V - E_{Na}) - 4a^4 \bar{g}_{KLT}(1 - U)^3 z_0(V - E_K) \right), \quad (8)$$

for the phasic model and only the first term in the expression above for the tonic model.

Notice that both terms on the right-hand side of equation (8) are negative for any value of  $V$  and  $t$  in the domain of study and therefore the above derivative is always nonzero. Then, by the implicit function theorem there exists a function  $\mathcal{U}$

defined on this domain such that

$$I(t) = I_{\text{ion}}(V, \mathcal{U}(V, t)).$$

Taking derivatives with respect to time  $t$  in the equation above we have that

$$\frac{dI}{dt} = \frac{\partial I_{\text{ion}}}{\partial U}(V, \mathcal{U}(V, t)) \frac{\partial \mathcal{U}}{\partial t}(V, t)$$

and since the term (8) does not vanish we can write

$$\frac{\partial \mathcal{U}}{\partial t}(V, t) = \left( \frac{\partial I_{\text{ion}}}{\partial U}(V, \mathcal{U}(V, t)) \right)^{-1} \frac{dI}{dt}. \quad (9)$$

Since the term in the denominator of equation (9) is negative, one can read from equation (9) that  $U$  on the  $V$ -nullcline decreases ( $\partial \mathcal{U} / \partial t < 0$ ) as  $I$  increases ( $dI/dt > 0$ ) and vice versa. Moreover, the decreasing speed of  $U$  depends on how fast  $I$  increases.

Of course, the formula for the  $V$ -nullcline sensitivity to  $I$  is consistent with the visual effects seen in Fig. 4C. First, let us look at the term in the denominator of equation (9) given explicitly in equation (8). Notice that the larger the denominator in (9), the smaller the sensitivity of the  $V$ -nullcline to the input changes. For  $V$  greater than about -40 mV,  $I_{\text{Na}}$  is fully activated ( $m_{\infty}(V)$  is near one) and the first term in equation (8) is large and dominates the expression for the denominator of (9). Hence the  $U$  value on the  $V$ -nullcline changes little with  $I$  in this  $V$ -range. In contrast, for the  $V$ -range that surrounds the left knee ( $V < -40$  mV) the first term in equation (8) is very small. Thus, for the tonic case (second term in equation (8) is zero) the  $V$ -nullcline is very sensitive to  $I$  around the left knee. For the phasic case this sensitivity is reduced by the contribution of the second term, due to the  $V$ -dependent gating of  $I_{\text{KLT}}$ . We see this difference in sensitivity (greater in the tonic case) in the phase plane plots. In the phasic case (Fig. 4C) the left knee drops by about 0.4 units in  $U$  as  $I$  increases by a large amount (1200 pA) while in the tonic case (Fig. 4C) the drop is much larger for a smaller increase in  $I$ .

Let us now look at equation (9) from the viewpoint of the dynamic criterion for spike generation. In the phase plane we need  $\partial \mathcal{U} / \partial t$  around the left knee to be large enough. If the  $\partial I_{\text{ion}} / \partial U$  is more negative (the phasic case) then  $dI/dt$  must be more positive to satisfy the criterion. This says that for the phasic model we need  $dI/dt$  larger than that for the tonic model (assuming similar threshold speed for  $\partial \mathcal{U} / \partial t$ ). We confirm with the formula that the phasic model is more sensitive to the input's rising speed than is the tonic model. Furthermore, the temporal window for spike generation is much smaller in the phasic case. As the stimulus slows down around its peak, the steady state is stable but the tonic model still has an opportunity to spike since the steady state can be on the middle branch and unstable.

These dynamical differences of the  $V$ -nullcline between the phasic and the tonic model are consistent with our biophysical intuition. In the phasic case, during a depolarizing stimulus,  $g_{\text{KLT}}$  can be recruited so that it compensates the depolarizing input current. The increased membrane conductance shunts the input current and the change in the  $V$ -nullcline is diminished compared to the tonic model.

**2.2.4. ISPD tuning curve.** The  $V$ - $U$  reduction has similar phase-locking and ISPD-tuning properties as the full RM03 model. The phase-locking response diagram (Fig. 5A) extends over the same range of stimulus parameter values as in Fig. 1 and shows near-quantitative reproducibility. The ISPD tuning curves (Fig. 5B) show striking similarity and sharp temporal precision to those for the RM03 model

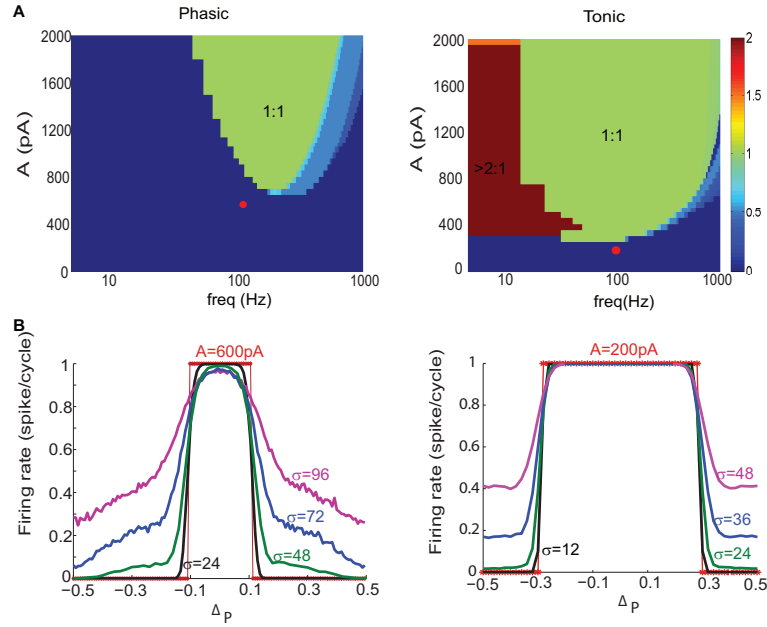


FIGURE 5. Phase-locking and coincidence detection for the V-U model. (A) Frequency-response maps of the phasic (left) and tonic (right) V-U models, corresponding to dynamic and frozen  $g_{KLT}$ , respectively. Colors represent spiking ratios (number of spikes per cycle) to half-wave rectified sinusoidal current inputs, equation (4), with varying frequency ( $x$ -axis) and amplitude ( $y$ -axis). Compare with Fig. 1 for the full RM03 model. (B) ISPD tuning curves for the phasic (left) and tonic (right) V-U model for 100Hz input. Different curves correspond to different noise levels  $\sigma$ . For the phasic model the sinusoidal amplitude is  $A=600\text{pA}$  and the noise level  $\sigma=0\text{pA}$ , 24 pA, 48 pA, 72 pA, 96 pA and for the tonic model  $A=300\text{pA}$  and  $\sigma=0\text{pA}$ , 12 pA, 24 pA, 36 pA, 48 pA, respectively.

for the same parameter values. The noise-free phasic model's tuning curve extends over  $\pm 0.1$  ISPD. For the tonic model it is much wider (Fig. 5B).

Additive noise leads to firing probability outside the deterministic window for firing as for the RM03 model (compare Fig. 5B with Fig. 2B). The V-U model fires more than does RM03 in the tails of the ISPD-tuning curve for the same noise level. This is because in the V-U model, we set  $m = m_\infty$ , making the model more responsive to depolarizing inputs. The V-U model captures the sharp decrease in firing rate near the boundary of the ISPD deterministic response window. For these comparisons we restricted the range of noise amplitude for the tonic model.

We can further quantify the dynamics of coincidence detection for the V-U model by examining in more detail the dynamical changes in the phase plane portrait during one cycle of the sinusoidal stimulus pair. Here, we add to our phase plane analysis for the phasic model (Fig. 4C) an effective or quasi-threshold separatrix, QTS (dashed green curves in Fig 6A), a concept introduced by FitzHugh [9] and used recently by Prescott [24]. The QTS (the trajectory that crosses the  $V$ -nullcline



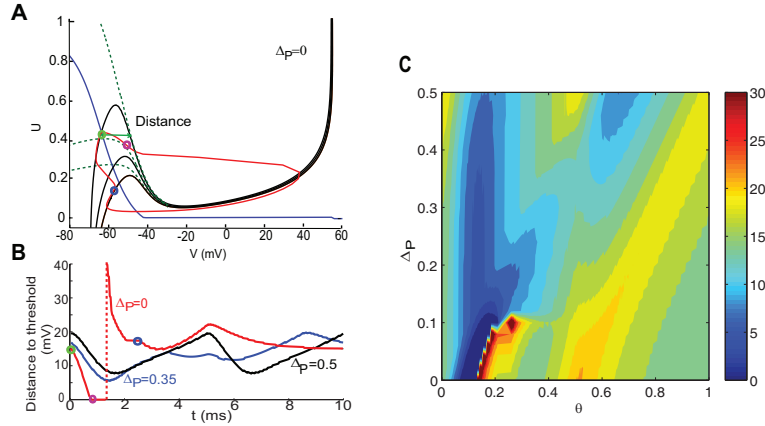


FIGURE 6. Dynamical analysis of the distance to threshold separatrix for the phasic V-U model. (A) Phase-plane analysis for a paired half-wave rectified sinusoidal input, equation (5), when  $\Delta_P = 0$ . The V-nullclines correspond to snapshots for  $I = 0, 600, 1200$  pA. The dashed trajectory lying alongside the middle branch of the V-nullcline is the quasi-threshold separatrix, QTS. (B) Horizontal distance from the  $(V, U)$  phase point to the QTS over one period of the input for  $\Delta_P = 0$  (red), 0.35 (blue), 0.5 (black). The colored dots denote the same system states as those on the trajectory of (A) for  $\Delta_P = 0$ . (C) Contour plot for the distance to the QTS at different phases during one cycle of the sinusoidal stimulus pair as  $\Delta_P$  varies. Colors correspond to the distance to threshold.

at the right knee) segregates state points for which the response trajectory returns to the steady state directly without a spike from those which lead to a spike. The QTS is computed by integrating backwards the trajectory starting at the lower turning point (right knee) of the V-nullcline. Although the  $V - U$  system does not have a strong time-scale separation, we have chosen this starting point in the middle branch so that if the system is turned into a slow-fast system by slowing down the variable  $U$ , the QTS coincides with the slow repelling manifold (the so-called excitation threshold boundary for a system with relaxation dynamics). In a slow-fast system the excitability threshold hugs the middle branch of the V-nullcline and turns leftward becoming horizontal above the left knee. Our computed QTS hugs the middle branch for a while (there is a strong time-scale separation in this region) but then overshoots the left knee to head north-northwest for modest  $I_{app}$  (in this region the two time-scales are comparable).

We use the horizontal distance of the  $(V, U)$  state to the QTS at each time step as a measure of the ease to fire a spike. The smaller the distance is, the easier it is for noise to trigger a spike. Here, in Fig. 6A,  $\Delta_P = 0$  and  $I_{max} = 1200$  pA for the combined sinusoidal input (equation (5)). When the stimulus begins,  $I = 0$  pA and the resting state is on the left side of the QTS. As  $I(t)$  rises, the V-nullcline drifts downwards and simultaneously the upper part of the QTS curves left and downwards, like an inverted U-shape. The fate of the trajectory from the resting state depends on how fast the stimulus increases, as we described earlier for Fig.

4C. For the case illustrated here both the  $V$ -nullcline and the QTS drop fast enough during the rising phase of  $I(t)$  relative to the trajectory of  $(V, U)$  (which depends on integrating the stimulus) so that the QTS sweeps downward across the  $(V, U)$  point during the rising phase of the current input. Correspondingly, the distance to the QTS (red, Fig. 6B) decreases to 0 within a short time (red, Fig. 6C) during the rising phase of the sinusoidal stimulus. The spike upstroke occurs just after the  $(V, U)$  point is outside the moving steady state's domain of attraction. After the spike, during the refractory period, the distance to threshold jumps to a very high value and decreases gradually to a level around 10 mV at the cycle's end. Thus, it becomes much more difficult for the noise to trigger another spike after the first one. For the paired sinusoidal stimulus, equation (5) with large  $\Delta_P$ , say phase shifted by 0.35 or 0.5, the trajectory remains in the steady state's domain of attraction to the left of and below the QTS. The distance to threshold first decreases as  $I$  increases and arrives at its minimum value before the current reaches  $I_{max}$ . Then it increases again (blue and black, Fig. 6C). A contour plot (Fig. 6C) shows the distance throughout the stimulus cycle for all  $\Delta_P$ . It can be seen that the minimum distances are reached during the rising phase for the phasic V-U model. However, for the tonic case, the minimal distance to threshold occurs around the maximum value of  $I(t)$  (not shown). Thus the phases for which firing occurs for the phasic model are quite concentrated in the rising phase of the stimulus (see the firing phase histograms in Appendix C Fig. 10). In contrast, the possible firing phases under noise for the tonic model are distributed broadly around the peak of the stimulus (Appendix C Fig. 10). The V-U model captures well these and the other features of the histograms that were found for the RM03 model (compare Appendix C Fig. 10 with Fig. 3). The distance to threshold is near minimum (contour plot, Fig. 6C), consistent with the interval for preferred firing phases; compare, say for  $\Delta_P = 0.25$  and 0.35 the blue region and the two blue regions for  $\Delta_P = 0.5$  in Fig. 6C with the corresponding panels in Appendix C Fig. 10, left.

**2.3.  $V - \theta$  model.** We develop an idealized model for Type III excitability in the form of a Leaky Integrate-and-Fire (LIF) model with a dynamic threshold  $\theta$ . We replace the conductance mechanism of RM03 for a subthreshold negative feedback by a dynamic threshold  $\theta$  that can rise with the subthreshold voltage  $V$ . Our model is a modification of the  $V - \theta$  model introduced in [8] to illustrate the phenomenon of Post-inhibitory Facilitation (PIF). Another version of this model, consisting of an exponential integrate-and-fire model with a non-linear equation for the dynamic threshold, was recently proposed in [22]. The main feature of these models is that, as opposed to many other models with dynamic threshold [18, 17], the threshold  $\theta$  can rise before the system reaches the spiking threshold.

The equations for the dimensionless system have the following form:

$$\begin{aligned} \frac{dV}{dt} &= -V + V_r + I(t) \\ \frac{d\theta}{dt} &= -\frac{\theta - f(V)}{\tau_\theta} \end{aligned} \quad (10)$$

where  $f(V) = a + \exp(b(V - c))$  is the steady state value of the threshold  $\theta$  at a voltage  $V$ ;  $\tau_\theta$  is the time constant for the threshold (which will be chosen only a bit slower than the membrane time constant, i.e.  $\tau_\theta > 1$ );  $V_r$  is the voltage at the resting state and  $I(t)$  is the injected current.

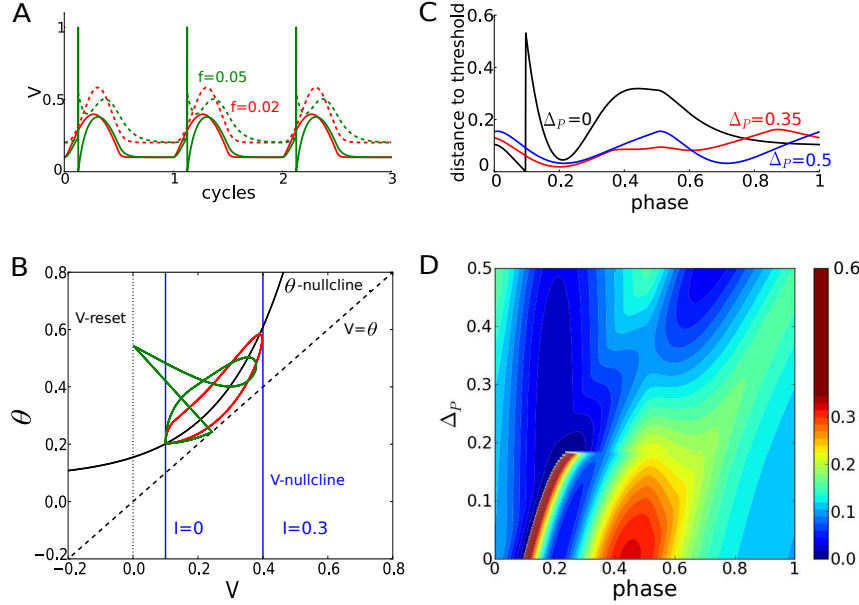


FIGURE 7. Dynamics of threshold and distance to threshold for the  $V-\theta$  model. (A) Time courses of the membrane voltage (solid lines) and spike threshold (dashed lines) over three periods in response to an input consisting of a single half-wave rectified sinusoid of  $A = 0.3$  and  $\omega = 0.05$  (green) and  $\omega = 0.02$  (red). In the firing case we have added vertical lines to emphasize the spike times. (B) Orbits of the firing and non-firing cases in A plotted on the  $V-\theta$  phase-plane. Nullclines for the minimum and maximum values of the input are shown. A spike occurs when the orbit crosses the line  $V = \theta$ . (C) Distance to threshold as a function of the input phase for an input of the form (5) with  $\omega = 0.05$  and  $A = 0.2$  and for different phase shifts  $\Delta_P$ . (D) Distance to threshold as a function of the input phase (x-axis) and phase shift  $\Delta_P$  (y-axis) for an input of the form (5) with  $\omega = 0.05$  and  $A = 0.2$ .

As is standard for LIF models we specify post-spike resetting conditions: if  $V(t^-) = \theta(t^-)$ , then  $V(t^+) = V_{\text{reset}}$  and  $\theta(t^+) = \theta(t^-) + \Delta_\theta$ , and we record one spike event.

In [8] the function  $f(V)$ , which determines the steady state value for  $\theta$  at a holding voltage  $V$ , was a linear function in  $V$ . Here, we have chosen a function  $f$  so that the curve of distance-to-threshold versus voltage has a non-monotonic shape (see the  $\theta$ -nullcline in Fig. 7B). Indeed, the distance is reduced when the cell is moderately depolarized ( $I$  small) and increased when the cell is further depolarized ( $I$  large). This leads to a non-monotonic firing rate probability function, which is a special signature of phasic models [12]. Moreover our system shows phasic behavior for the whole range of  $I$ .

The parameters of the system are  $V_r = 0.1$ ,  $V_{\text{reset}} = 0$ ,  $\Delta_\theta = 0.3$ ,  $a = 0.08$ ,  $b = 4.9$ ,  $c = 0.53$  and  $\tau_\theta = 2$ .

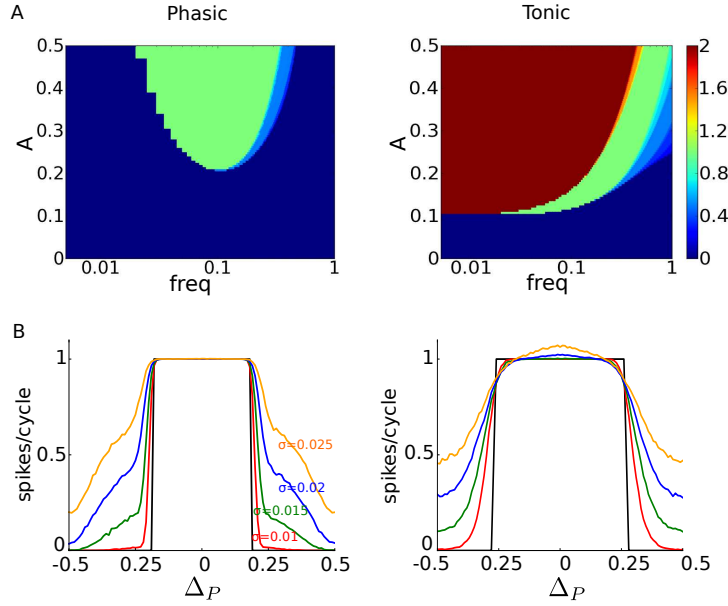


FIGURE 8. Phase-locking and coincidence detection for the  $V - \theta$  model. (A) Frequency-response diagrams of the  $V - \theta$  models phasic (left) and tonic (right) for a half-wave rectified sinusoidal input with varying frequency (x-axis) and amplitude (y-axis). Colors indicate number of spikes per cycle. (B) ISPD tuning curves for phasic (left) and tonic (right)  $V - \theta$  models. Plots show the spiking ratio (spikes/cycle) in response to an input current consisting of two half-wave rectified sinusoids with varying phase shift  $\Delta_P$  for the deterministic case (black curve) and for different levels of noise ( $\sigma = 0.01, 0.015, 0.02, 0.025$  corresponding to red, green, blue and yellow curves respectively). The frequencies for a single half-wave rectified sinusoid are 0.05 (phasic) and 0.2 (tonic) and the amplitudes are 0.2 (phasic) and 0.1 (tonic).

If  $\theta$  is frozen at its value at the resting state the model is a standard LIF, and the system shows tonic behavior (pseudo Type I) when the input is raised above the threshold.

**2.3.1. The idealized  $V - \theta$  model shows Type III excitability.** Notice that for all values of  $I$  the system has a unique stable fixed point that is subthreshold. It corresponds to the intersection of the  $\theta$ -nullcline ( $f$  function) with the  $V$ -nullcline (vertical lines  $V = I + V_0$ ), i.e.  $(I + V_0, f(I + V_0))$  (Fig. 7B). The fixed point is a stable node with eigenvalues  $\lambda_1 = -1$  and  $\lambda_2 = -1/\tau_\theta$  and associated eigenvectors  $v_1 = (1, f'(I + V_r)/\tau_\theta)$  and  $v_2 = (0, 1)$ . When the system is depolarized, the trajectory will move towards the holding state (fixed point). Since we have chosen  $\tau_\theta > 1$ , the trajectory on the phase plane will move towards the  $V$ -nullcline first and ultimately become tangent to it.

Because of the choice of the function  $f$ , if  $I$  increases slowly, the voltage  $V$  increases at a slow rate allowing the threshold to rise and the trajectory never

crosses the line  $V = \theta$  (Fig. 7B and Fig. 7A., red curves). However, fast changes in  $I$  cause the  $(V, \theta)$  state point to cross the line  $V = \theta$  before the threshold has had time to rise enough (Fig. 7B and Fig. 7A, green curves).

After one spike has occurred the system is reset to the  $V_{\text{reset}}$  line and the system's trajectory will approach the fixed point, which is on the left hand side of the firing line  $V = \theta$ . In the biophysical models, RM03 and V-U, a spike event recruits more  $I_{\text{KLT}}$ , raising even more the threshold for eliciting a spike. We implemented this idea by raising the threshold by a magnitude  $\Delta_\theta$  after a spike has occurred. The value of  $\Delta_\theta$  and  $\tau_\theta$  determine the number of times the trajectory hits the firing line before it reaches the fixed point. For our simulations we have chosen values for which the system triggers only one spike during this transient phase.

**2.3.2. ISPD tuning curves and phase locking.** The tonic (standard LIF model) and phasic models ( $V - \theta$  model) reproduce qualitatively the same properties as the two biophysical models discussed in the previous sections.

In Fig. 8A we show the frequency response of the system when  $I(t)$  is a half-wave rectified sinusoid (equation (4)). As for the tonic RM03 our tonic model shows a critical amplitude of the input that causes firing and this remains constant for low frequencies. Notice that since the threshold is fixed at  $\theta = 0.2$  it is very easy to see from equations (10) that the critical amplitude to cross the threshold is 0.1. In contrast, for the phasic model the frequency response shows a clear dependence on the frequency. As in RM03, the system does not respond for very low frequencies (for the amplitudes tested); firing occurs only when the combination of amplitude and frequency of input produces a fast enough rise (steep slope).

We also computed the ISPD tuning curves (both deterministic and with added white noise) for the tonic and phasic  $V - \theta$  models (see Fig. 8). We chose an amplitude and frequency using the same criterion as we did when computing the RM03 ISPD tuning curves. When noise is added, the ISPD tuning curves show a characteristic signature of the type of model: for tonic ISPDs the firing rate is substantial and stays constant for values of  $\Delta_P$  higher than  $1/3$ , whereas for phasic ISPDs the firing rate is kept low and decreases in the tails.

The firing phase and interspike interval histograms reproduce qualitatively the distributions and features obtained for RM03. The phasic model shows higher vector strength (better phase locking) than the tonic model; the response in the phasic model occurs during the rising phase of the input whereas in the tonic model it takes place around the peak of the input; the tonic model shows more dispersion in the ISI histograms than the phasic model.

The  $V - \theta$  model has a definite threshold that allows us to compute explicitly the distance to threshold for different inputs. In Fig. 7C we show the distance to threshold as a function of the phase for three different values of  $\Delta_P$  (compare with Fig. 6B). Notice that the reduced  $V - \theta$  model captures the qualitative features obtained for the V-U reduction of the RM03 model (see Fig. 6B), such that the distance is shorter in the rising phase of the input and that this distance increases as the depolarizing input is maintained. Notice also that during the pause phase (stimulus is off) this distance is shortened: the longer is the pause the shorter is the distance to threshold at the onset of the input. The same features can be observed in Fig. 7D, which is analogous to Fig. 6C.

**3. Discussion.** Some neurons and neuron models do not fire repetitively for steady or slow inputs. They fire in response to fast enough rising inputs only, say at the

onset of a steady input. This property of phasic firing is called Type III excitability [16, 24]. Correspondingly, the resting state remains stable for any value of a steady input that is physiologically plausible. The underlying mechanism is a subthreshold negative feedback, voltage-gated and recruited dynamically, that can hinder spike generation for slow inputs. Hence, for Type III excitability firing occurs only when the voltage can outrace the negative feedback before this feedback can fully activate. Such neurons and neuron models can act as slope detectors. They are well-suited for temporal processing like phase-locking and coincidence detection and with extraordinary temporal precision if the feedback can be recruited on a time scale that is comparable to the membrane time constant.

We have considered a model (RM03) for neurons in the auditory brainstem that shows Type III excitability [32]. The underlying mechanism is a low-threshold activated potassium current  $I_{\text{KLT}}$  that at the resting state has a time scale of activation that is comparable to the membrane time constant. When the  $I_{\text{KLT}}$  current's conductance is frozen at its resting value the dynamics of the subthreshold negative feedback are disabled. The modified model behaves tonically, able to fire repetitively, over a certain range of input current values  $I$ . We have compared the ability of the original model (phasic) and the modified one (tonic) to phase lock and to perform coincidence detection. Our results show that phasic neurons have better temporal precision, including when white noise is added to the input.

We have provided insight into the coincidence detection performance of RM03 and Type III systems more generally by developing and analyzing two different reduced models that reproduce qualitatively the dynamics of the exemplar model, RM03, in both phasic and tonic regimes. Our results underscore the importance of Type III excitability for precise coincidence detection.

**3.1. Two-variable models.** Each of our reduced models has just two variables. This allowed us to use phase plane analysis and to provide a geometrical interpretation for various features, such as: stability of the steady state and sensitivity of nullclines to changes in  $I$ , nearness to threshold, and the temporal integration window. For our reduced models we were able to detect and quantify the size of a temporal window for firing as the input signal changes in time. We found that the phasic models show higher selectivity to an input's rising slope than do the tonic models. Thus, in our phasic models the size of the temporal window for firing shrinks when the signal's slope is reduced, whereas for the tonic models firing can still occur even if the input slows to a crawl. Eventually, the input amplitude will enter into the tonic model's regime for repetitive firing.

**3.1.1.  $V$ - $U$  model, a reduction of the RM03 model.** We applied time scale separation and approximation arguments to directly reduce the RM03 model to two variables and thereby retain biophysical parameters in the reduced model. The phasic version incorporates dynamic negative feedback through the variable  $U$  in two gating processes: activation of  $I_{\text{KLT}}$  and inactivation of  $I_{\text{Na}}$ .

The phase plane portraits of our  $V$ - $U$  model have the characteristic shape of systems for which the negative feedback is dominated by inactivation of an inward current (the vertically flipped  $V$ -nullcline). We chose this representation because when we convert the  $V$ - $U$  model to tonic mode, the dynamic negative feedback is due only to inactivation of  $I_{\text{Na}}$ . Hence, the nullclines look similar for both models although they differ quantitatively and have different sensitivities to  $I$ . The phase plane portraits resemble those of models for the low-threshold spike in thalamic

neurons, mediated by an inactivating or transient inward (calcium) current (see, e.g., [31]). Our analysis of the  $V$ -nullcline's left knee and its strong sensitivity to  $I$  would also apply to those models, with weak or no voltage-dependent potassium currents.

We could have recast the formulation of the phasic model with  $w$  being proportional to  $U$  and obtained the more familiar appearance of nullclines where the negative feedback is increasing during a spike, as in the Morris-Lecar model [30]. In either case, the  $V$ - $U$  model provides a simple enough system to study and still be able to relate with some biophysical plausibility to the functional significance of Type III excitability and to the neuronal computation of coincidence detection.

Our reduction and analysis benefited from key observations of FitzHugh [9, 10] of the dynamics of excitability in the HH model and in his BVP model (now called the FitzHugh-Nagumo model). He noted the near linear relationship of  $h$  and  $n$  in the HH model. He introduced the notion of the quasi-threshold separatrix. This notion has also been used effectively by Prescott *et al* [24] in their treatment of Type III excitability for two-variable models.

**3.1.2.  $V - \theta$  model, an idealization of the RM03 model.** The main feature of our  $V - \theta$  model is a dynamic threshold that can vary with voltage in the subthreshold regime. This idea was previously implemented in [8] to illustrate and to explain Post-Inhibitory Facilitation (PIF) in the RM03 model. The PIF effect occurs when brief inhibition (being delivered within a proper time window before excitation) facilitates the generation of a spike. The conductance mechanism responsible for the PIF effect was implemented in the LIF framework by using a dynamic threshold that decreased when the system was hyperpolarized. The dynamics for the threshold  $\theta$  was designed so that the system could reproduce the mentioned effect over a limited range of  $I$ 's, for which the system showed phasic behavior.

In this paper we modified the dynamics of  $\theta$  so that the  $V - \theta$  model shows phasic behavior over the whole range of applied currents  $I$  (the resting point remains stable) with slope sensitivity (the system elicits a spike only if the input is fast enough).

The dynamic threshold for the LIF models has been widely used to implement superthreshold negative feedback (such as spike frequency adaptation) [17, 18]. In contrast to our  $V - \theta$  model, the dynamic effects on the threshold are due to the spiking and not to subthreshold fluctuations of the voltage  $V$ . Other LIF models implement subthreshold negative feedback (such as subthreshold adaptation) by adding a second equation which describes adaptation but keeping a fixed threshold; see [27] and also the adaptive exponential integrate-and-fire model (aEIF) [2] (for a certain range of the parameters).

**3.2. Biophysical mechanisms for a dynamic subthreshold negative feedback.** There are several possible cellular mechanisms that prevent the destabilization of the resting state and the generation of multiple spikes, producing Type III excitability.

In this paper we have discussed a subtractive mechanism (a low-threshold  $K^+$  current) as responsible for preventing repetitive firing. When the cell depolarizes slowly, the  $K^+$  current (that activates for subthreshold values of the voltage) has enough time to activate and oppose the voltage rise, keeping the membrane voltage subthreshold. In contrast, when the depolarization is fast enough due to a fast-rising input current, the  $K^+$  current does not have time to activate and the system



can elicit a spike. During the spike, the  $K^+$  current activates fast preventing the generation of a subsequent spike.

Although Type III excitability is often associated with a subtractive mechanism (outward  $K^+$  currents, [5, 24]) this is not the only possible biophysical mechanism to generate a subthreshold negative feedback. A divisive mechanism, such as a fast-activating, but transient, inward (sodium or calcium) current with suitably recruitable inactivation, can also generate Type III excitability. The conceptual framework is the same. If the cell depolarizes slowly, the inactivation process develops before the inward current can activate and the cell will not fire a spike. If the depolarization is fast enough before inactivation of the inward current can occur, a spike (and only one spike) is produced. Indeed our V-U model can show Type III excitability with the  $I_{KLT}$  conductance frozen and sodium inactivation gating somewhat re-tuned [21]. In some auditory neurons both subtractive and divisive mechanisms [34, 38] contribute to phasic firing; it appears that inactivation of  $I_{Na}$  is V-gated at unusually lower V values. The possibility of both mechanisms being available raises interesting questions about how the system might use them to advantage.

An important aspect, whether the mechanism is subtractive or divisive, is that time constant of the associated gating variable be neither too fast or too slow in order to achieve excitability and temporally precise coincidence detection. Consider the case of  $I_{KLT}$ . Indeed, if  $\tau_w$  (the time constant for the activation of  $I_{KLT}$ ) is too small,  $I_{KLT}$  would prevent the generation of a spike even for faster input currents and the system will no longer be excitable. On the contrary, if  $\tau_w$  is too large, the critical input slope for generating a spike would decrease, therefore reducing the ability of these cells to detect coincident inputs. Hence, when  $\tau_w$  is increased the frequency window (say, for the phase-locking 1:1 region in Fig. 1C) broadens, especially on the low frequency side. The ISPD tuning curves also broaden, reducing the coincidence detection selectivity of the cell.

**3.3. Type III excitability and neuronal computation.** Type III excitability explains the extremely precise temporal computations of the MSO neurons in the auditory brain stem. MSO neurons receive inputs originating in both ears and are capable of detecting time differences in the arrival of those inputs on the order of tens of microseconds. This is a surprising property taking into account that their spike and synaptic response widths and membrane time constants are ten times larger.

We have shown that Type III excitability, phasic firing, (a characteristic signature of MSO neurons) requires the input to be fast enough to overcome the subthreshold negative feedback and generate a spike. Hence, these neurons are very responsive to bilateral inputs, each subthreshold, that arrive nearly synchronously (short rise time) while they do not show any response when arriving with a small time shift (longer rise time). The key point is that the MSO neurons are responding primarily to the steepness of the rising input, and not to the duration or amplitude of the input (if not fast enough). This is how they can achieve a time resolution faster than the membrane constant. The tuning curves for coincidence detection of the RM03 model, for our idealized paired inputs, show a dramatic drop in the firing rate over a change in ISTD of 10-100  $\mu$ s. This temporal resolution may be even sharper for inputs that mimic more realistically what is carried by the auditory nerve for a pure tone stimulus; the spike probability waveform per cycle on the auditory nerve has a much faster rising phase than falling phase. At least two factors contribute

to the drop in firing probability as  $\Delta_P$  increases in the tails of the ISPD-tuning curves for phasic models. The rising slope of the input decreases and there may be considerable negative feedback generated even by subthreshold voltage responses at moderate input rates (like our 100 Hz examples).

Our illustrations of temporally precise coincidence detection have been for moderate frequencies (order, 100 Hz). For low frequencies the noise-free phasic models do not spike although with some probability they do spike in the presence of noise. This suggests a stochastic resonance basis; however, the form is not classical. The phasic models do not fire because of noise around the peak of (an otherwise subthreshold) sinusoidal input but rather on the rising slope. This slope-based stochastic resonance is still mediated by the Type III excitability of RM03; the tonic version shows classical, amplitude-based stochastic resonance [12]. This behavior has implications for localization of slowly modulated sounds whose carrier frequencies exceed the ability of MSO neurons to phase-lock [11]. We did not address the dependence of coincidence detection for increasing amplitude and frequency, where precise temporal processing may be compromised; some effects have been studied in vitro [6, 26]. These increases can promote firing in the anti-phase troughs of the tuning curves, corresponding to an increased number of “false positive” responses in a sound localization task.

Many other neuron types exhibit Type III excitability (see Discussion in [24]), for example, some neurons in the spinal cord. Some stretch receptors adapt rapidly

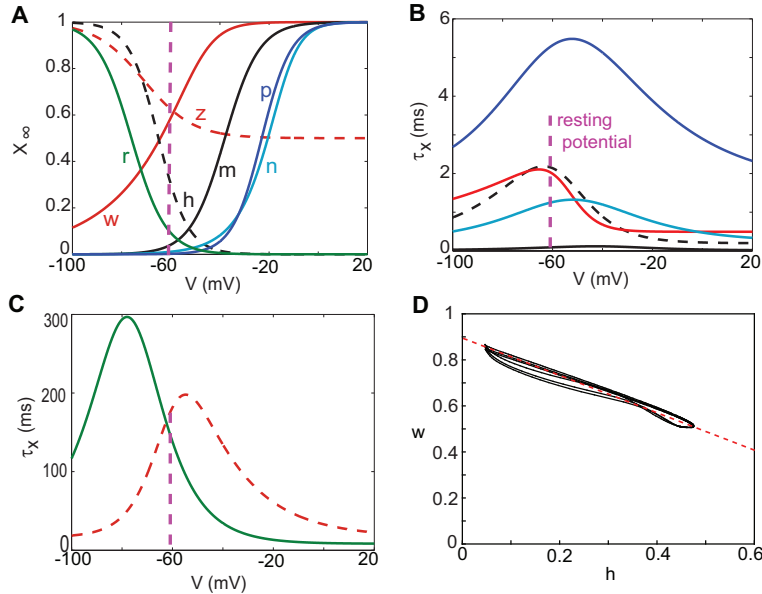


FIGURE 9. The voltage-dependent steady-state functions (A) and time constant functions (B, C) for the gating variables of the ionic currents in the RM03 model (1). Solid and dashed lines stand for activation and inactivation gating variables, respectively. (D) Trajectory of the RM03 model during spikes projected on the  $w-h$  plane;  $w$  and  $h$  co-vary linearly

(phasic) and some tonically, presumably for signalling stimulus onset (and perhaps offset) and for stimulus intensity [35].

The impressive temporal processing capability of phasic auditory brain stem neurons is compelling, especially because we know that they play a primary role in computing interaural time difference for sound localization. While we have used phase plane methods and notions of phase-locking from dynamical systems theory, other approaches to study the responsiveness of phasic models and neurons to fluctuating inputs have included reverse correlation methods [7, 36]. The further mathematical characterization of Type III excitability and additional implications for neuronal computation lie ahead.

**Appendix A. Numerical methods.** The noise-free RM03 dynamical equations (2-3) were integrated using an implicit 4th order Runge-Kutta method with a tolerance of  $10^{-7}$ . The  $V-\theta$  (10) and the  $V-U$  (6) dynamical equations were integrated using a forward Euler method with a time step of 0.005. Stochastic differential equations were integrated using a forward Euler method with a time step of 0.005 ms, along with a random generator that generated long non-repetitive series. In order to obtain a large dataset to analyze the stochastic response, we ran the simulations up to the order of  $10^4$  cycles of the signal. For the RM03 and V-U models spike times were recorded when the trajectory crossed the section  $V = -15$  upwards. The bifurcation diagrams were computed using the Auto feature in XPPAUT. We used Matlab and Python to analyze and plot the data.

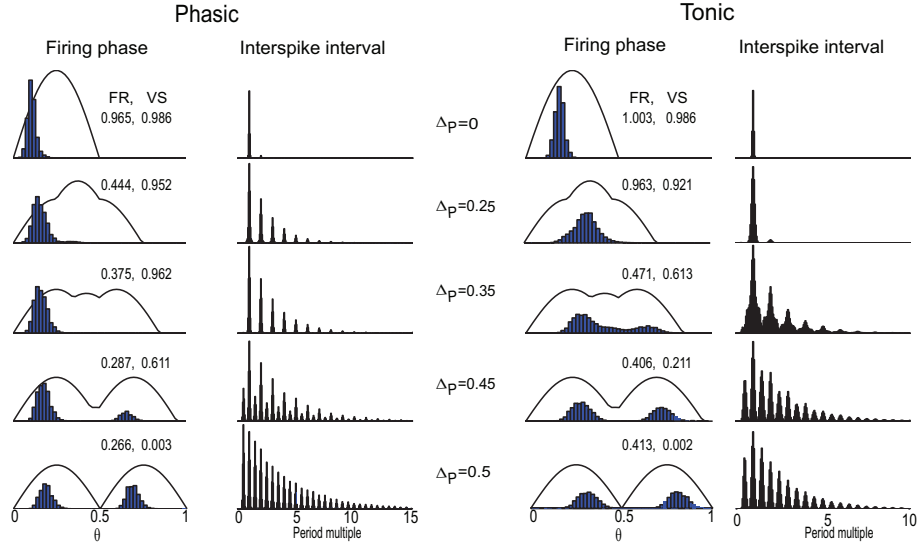


FIGURE 10. Normalized firing phase histograms and inter-spike interval (ISI) histograms for the phasic and tonic V-U models in response to two rectified sinusoids at different phase shifts  $\Delta_P$  with noise  $\sigma = 96\text{pA}$ . The frequency of a single half-wave rectified sinusoid is 100 Hz and the amplitude is 600 pA (phasic) and 200 pA (tonic). The curves in the firing phase histogram plots represent the time course of the input signal over one period.

**Appendix B. RM03 model.** The voltage-dependent steady-state functions of the gating variables in the RM03 model are shown in Fig. 9A. For a given voltage value  $V$ , the gating variables approach their steady state values with the time constants (also voltage-dependent) that are shown in Fig. 9B and C. The time constants are chosen to mimic the brain slices during whole cell recordings at temperature  $32^\circ\text{C}$ .

We notice that in the RM03 model, the activation gating variable  $w$  of  $I_{\text{KLT}}$  and the inactivation gating variable  $h$  of  $I_{\text{Na}}$  have similar time constant functions. They co-vary linearly during a spike (Fig. 9D). A decent fit for the relationship between  $w$  and  $h$  is provided by the line  $L$  (dashed, Fig. 9D):  $w + b \cdot h = a$ , where  $a = 0.9$  and the slope  $b = (a - w_0)/h_0$ ,  $w_0, h_0$  are the resting values of  $w$  and  $h$ ;  $L$  passes through the points:  $(h_0, w_0)$  and  $(0, a)$ . Motion along  $L$  is described by a single recovery variable  $U$  which is defined precisely by the linear combination:  $U = b[h + b(a - w)]/a(1 + b^2)$ . This representation was used by Rinzel in [29] for the HH reduction.

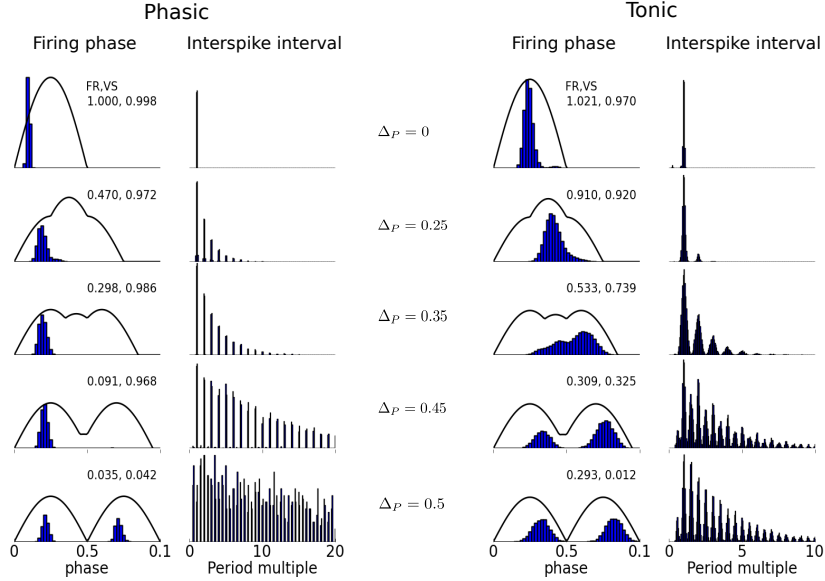


FIGURE 11. Phase histograms and inter-spike interval (ISI) histograms for the  $V - \theta$  phasic and tonic models in response to two half-wave rectified sinusoids at different phase shifts  $\Delta_P$  with noise  $\sigma = 0.02$ . A single input is a half-wave rectified sinusoid of  $f=0.05$  and  $A=0.2$  (phasic) and  $f=0.2$  and  $A=0.1$  (tonic). The curves in the phase histogram plots represent the time course of the input signal over one period. Phase histograms are normalized and the scale of the vertical axis is the same for all panels of each model. The scale of the vertical axis of the ISI histograms is different in each panel due to the large variation across panels. The numbers in the upper right corner of the phase histogram panels indicate firing rate (spikes/cycle) (FR) and vector strength (VS).

**Appendix C. Histograms of the  $V-U$  model and the  $V-\theta$  model.** The firing phase histograms and ISI histograms of the  $V-U$  model and the  $V-\theta$  model capture the characteristic features of the RM03 model in response to an input consisting of two half-wave rectified sinusoidal inputs with phase difference  $\Delta_P$  (equation (5)). See Fig. 3, 10 and 11 for RM03,  $V-U$  and  $V-\theta$  models respectively. The firing phase histograms show that for a phasic model spikes are concentrated in the rising phase of the stimulus whereas for a tonic model they are more dispersed around the peak. The vector strength for both models decreases as  $\Delta_P$  increases, but is higher in the phasic case. The ISI histograms decrease in an exponential way and the exponential decay decreases with  $\Delta_P$ . Notice that the phasic ISI histograms for the  $V-U$  model have a faster decay than the ones for RM03 as  $\Delta_P$  approaches 0.5. This is because the firing rate for the  $V-U$  model is much higher than that for the RM03 model for the same values of noise. We can observe this by looking at Fig. 5B and Fig. 2B. With the same noise amplitude  $\sigma = 96\text{pA}$  the ISPD tuning curve for the  $V-U$  model is much higher than that of the RM03 model. When we set  $\sigma = 72\text{pA}$  in the  $V-U$  model, we obtain similar histograms and firing rates as those in the RM03 model for  $\sigma = 96\text{pA}$  (results not shown).

**Acknowledgments.** We especially recognize, John Guckenheimer, for his interest in, support of, and contributions to the applications of dynamical systems theory to understanding neuronal systems.

The research for this study was supported, in part, by the National Institutes of Health grant DC008543-01 (JR and XYM), the National Natural Science Foundation of China grant 10872014 (XYM), an i-math Fellowship “Proyectos flechados” (GH), MICINN-FEDER grant MTM2009-06973 and CUR-DIUE grant 2009SGR859 (GH). GH wants to acknowledge the use of UPC Applied Math cluster system for research computing.

## REFERENCES

- [1] L. R. Bernstein, *Auditory processing of interaural timing information: New insights*, J. Neurosci. Res., **66**, (2001), 1035–1046.
- [2] R. Brette and W. Gerstner, *Adaptive exponential integrate-and-fire model as an effective description of neuronal activity*, J. Neurophysiol., **94** (2005), 3637–3642.
- [3] H. M. Brew and I. D. Forsythe, *Two voltage-dependent  $K^+$  conductances with complementary functions in postsynaptic integration at a central auditory synapse*, J. Neurosci., **15** (1995), 8011–8022.
- [4] C. E. Carr and K. M. Macleod, *Microseconds matter*, PLoS Biol., **8** (2010), e1000405.
- [5] J. R. Clay, D. Paydarfar and D. B. Forger, *A simple modification of the Hodgkin and Huxley equations explains type 3 excitability in squid giant axons*, J. R. Soc. Interface, **5** (2008), 1421–1428.
- [6] D. L. Cook, P. C. Schwindt, L. A. Grande and W. J. Spain, *Synaptic depression in the localization of sound*, Nature, **421** (2003), 66–70.
- [7] M. L. Day, B. Doiron and J. Rinzel, *Subthreshold  $K^+$  channel dynamics interact with stimulus spectrum to influence temporal coding in an auditory brain stem model*, J. Neurophysiol., **99** (2008), 534–544.
- [8] R. Dodla, G. Svirskis and J. Rinzel, *Well-timed, brief inhibition can promote spiking: Postinhibitory facilitation*, J. Neurophysiol., **95** (2006), 2664–2677.
- [9] R. Fitzhugh, *Impulses and physiological states in theoretical models of nerve membrane*, Biophys. J., **1** (1961), 445–466.
- [10] R. FitzHugh, *Mathematical models of excitation and propagation in nerve*, in “Biological Engineering” (ed. H. P. Schwan), McGraw-Hill Book Company, New York, (1969), 1–85.

- [11] Y. Gai, B. Doiron, V. Kotak and J. Rinzel, *Noise-gated encoding of slow inputs by auditory brain stem neurons with a low-threshold  $K^+$  current*, J. Neurophysiol., **102** (2009), 3447–3460.
- [12] Y. Gai, B. Doiron and J. Rinzel, *Slope-based stochastic resonance: How noise enables phasic neurons to encode slow signals*, PLoS Comput. Biol., **6** (2010), e1000825, 15 pp.
- [13] J. M. Goldberg and P. B. Brown, *Response of binaural neurons of dog superior olivary complex to dichotic tonal stimuli: Some physiological mechanisms of sound localization*, J. Neurophysiol., **32** (1969), 613–636.
- [14] R. Guttman, S. Lewis and J. Rinzel, *Control of repetitive firing in squid axon membrane as a model for a neuronoscillator*, J. Physiol. (Lond.), **305** (1980), 377–395.
- [15] A. L. Hodgkin, *The local electric changes associated with repetitive action in a non-medullated axon*, J. Physiol. (Lond.), **107** (1948), 165–181.
- [16] Eugene M. Izhikevich, “Dynamical Systems in Neuroscience: The Geometry of Excitability and Bursting,” Computational Neuroscience, MIT Press, Cambridge, MA, 2007.
- [17] B. Lindner and A. Longtin, *Effect of an exponentially decaying threshold on the firing statistics of a stochastic integrate-and-fire neuron*, J. Theor. Biol., **232** (2005), 505–521.
- [18] Y. H. Liu and X. J. Wang, *Spike-frequency adaptation of a generalized leaky integrate-and-fire model neuron*, J. Comput. Neurosci., **10** (2001), 25–45.
- [19] P. B. Manis and S. O. Marx, *Outward currents in isolated ventral cochlear nucleus neurons*, J. Neurosci., **11** (1991), 2865–2880.
- [20] X. Meng, Q. Lu and J. Rinzel, *Control of firing patterns by two transient potassium currents: Leading spike, latency, bistability*, J. Comput. Neurosci., **31** (2010), 117–136.
- [21] X. Y. Meng and J. Rinzel, *A two-variable reduction of the Rothman-Manis model for phasic firing*, Abstracts of the Thirty-Fourth Annual Mid-Winter Research Meeting of the Association for Research in Otolaryngology, **34** (2011), 154.
- [22] J. Platkiewicz and R. Brette, *A threshold equation for action potential initiation*, PLoS Comput. Biol., **6** (2010), e1000850, 16 pp.
- [23] S. A. Prescott and Y. De Koninck, *Four cell types with distinctive membrane properties and morphologies in lamina I of the spinal dorsal horn of the adult rat*, J. Physiol. (Lond.), **539** (2002), 817–836.
- [24] S. A. Prescott, Y. De Koninck and T. J. Sejnowski, *Biophysical basis for three distinct dynamical mechanisms of action potential initiation*, PLoS Comput. Biol., **4** (2008), e1000198, 18 pp.
- [25] M. Rathouz and L. Trussell, *Characterization of outward currents in neurons of the avian nucleus magnocellularis*, J. Neurophysiol., **80** (1998), 2824–2835.
- [26] A. D. Reyes, E. W. Rubel and W. J. Spain, *In vitro analysis of optimal stimuli for phase-locking and time-delayed modulation of firing in avian nucleus laminaris neurons*, J. Neurosci., **16** (1996), 993–1007.
- [27] M. J. Richardson, N. Brunel and V. Hakim, *From subthreshold to firing-rate resonance*, J. Neurophysiol., **89** (2003), 2538–2554.
- [28] J. Rinzel, *On repetitive activity in nerve*, Fed. Proc., **37** (1978), 2793–2802.
- [29] J. Rinzel, *Excitation dynamics: Insights from simplified membrane models*, Fed. Proc., **44** (1985), 2944–2946.
- [30] J. Rinzel and G. B. Ermentrout, *Analysis of neural excitability and oscillations*, in “Methods in Neuronal Modelling: From synapses to Networks” (eds. C. Koch and I. Segev), 2<sup>nd</sup> edition, MIT Press, Cambridge, MA, (1998), 251–291.
- [31] J. Rinzel, D. Terman, X. Wang and B. Ermentrout, *Propagating activity patterns in large-scale inhibitory neuronal networks*, Science, **279** (1998), 1351–1355.
- [32] J. S. Rothman and P. B. Manis, *The roles potassium currents play in regulating the electrical activity of ventral cochlear nucleus neurons*, J. Neurophysiol., **89** (2003), 3097–3113.
- [33] J. W. Schnupp and C. E. Carr, *On hearing with more than one ear: Lessons from evolution*, Nat. Neurosci., **12** (2009), 692–697.
- [34] L. L. Scott, P. J. Mathews and N. L. Golding, *Perisomatic voltage-gated sodium channels actively maintain linear synaptic integration in principal neurons of the medial superior olive*, J. Neurosci., **30** (2010), 2039–2050.
- [35] J. P. Segundo and O. Diez Martinez, *Dynamic and static hysteresis in crayfish stretch receptors*, Biol. Cybern., **52** (1985), 291–296.
- [36] S. J. Slee, M. H. Higgs, A. L. Fairhall and W. J. Spain, *Two-dimensional time coding in the auditory brainstem*, J. Neurosci., **25** (2005), 9978–9988.

- [37] G. Svirskis, V. Kotak, D. H. Sanes and J. Rinzel, *Enhancement of signal-to-noise ratio and phase locking for small inputs by a low-threshold outward current in auditory neurons*, J. Neurosci., **22** (2002), 11019–11025.
- [38] G. Svirskis, V. Kotak, D. H. Sanes and J. Rinzel, *Sodium along with low-threshold potassium currents enhance coincidence detection of subthreshold noisy signals in MSO neurons*, J. Neurophysiol., **91** (2004), 2465–2473.
- [39] T. Tatenos, A. Harsch and H. P. Robinson, *Threshold firing frequency-current relationships of neurons in rat somatosensory cortex: Type 1 and type 2 dynamics*, J. Neurophysiol., **92** (2004), 2283–2294.
- [40] X. J. Wang and G. Buzsaki, *Gamma oscillation by synaptic inhibition in a hippocampal interneuronal network model*, J. Neurosci., **16** (1996), 6402–6413.

Received May 2011; revised July 2011.

E-mail address: [lindamengxy@gmail.com](mailto:lindamengxy@gmail.com)

E-mail address: [gh707@nyu.edu](mailto:gh707@nyu.edu)

E-mail address: [rinzel@cns.nyu.edu](mailto:rinzel@cns.nyu.edu)